Radiative forcing from aircraft NOx emissions: Mechanisms and seasonal dependence

Radiative forcing from aircraft NO_x emissions: Mechanisms and seasonal dependence

David S. Stevenson and Ruth M. Doherty
Institute of Atmospheric and Environmental Science, University of Edinburgh, Edinburgh, Scotland, UK

Michael G. Sanderson, William J. Collins, and Colin E. Johnson
Hadley Centre for Climate Prediction and Research, Met Office, Exeter, Devon, UK

Richard G. Derwent
rdscientific, Newbury, Berkshire, UK

Received 11 March 2004; revised 7 June 2004; accepted 6 July 2004; published 14 September 2004.

[1] A chemistry-climate model has been applied to study the radiative forcings generated by aircraft NO_x emissions through changes in ozone and methane. Four numerical experiments, where an extra pulse of aircraft NO_x was emitted into the model atmosphere for a single month (January, April, July, or October), were compared to a control experiment, allowing the aircraft impact to be isolated. The extra NO_x produces a short-lived (few months) pulse of ozone that generates a positive radiative forcing. However, the NO_x and O_3 both generate OH, which leads to a reduction in CH_4. A detailed analysis of the OH budget reveals the spatial structure and chemical reactions responsible for the generation of the OH perturbation. Methane's long lifetime means that the CH_4 anomaly decays slowly (perturbation lifetime of 11.1 years). The negative CH_4 anomaly also has an associated negative O_3 anomaly, and both of these introduce a negative radiative forcing. There are important seasonal differences in the response of O_3 and CH_4 to aircraft NO_x, related to the annual cycle in photochemistry; the O_3 radiative forcing calculations also have a seasonal dependence. The long-term globally integrated annual mean net forcing calculated here is approximately zero, although earlier work suggests a small net positive forcing. The model design (e.g., upper tropospheric chemistry, convection parameterization) and experimental setup (pulse magnitude and duration) may somewhat influence the results: further work with a range of models is required to confirm these results quantitatively. *INDEX TERMS:* 0322 Atmospheric Composition and Structure: Constituent sources and sinks; 0345 Atmospheric Composition and Structure: Pollution—urban and regional (0305); 0365 Atmospheric Composition and Structure: Troposphere—composition and chemistry; 0368 Atmospheric Composition and Structure: Troposphere—constituent transport and chemistry; *KEYWORDS:* aircraft NO_x emissions, radiative forcing

Citation: Stevenson, D. S., R. M. Doherty, M. G. Sanderson, W. J. Collins, C. E. Johnson, and R. G. Derwent (2004), Radiative forcing from aircraft NO_x emissions: Mechanisms and seasonal dependence, *J. Geophys. Res.*, *109*, D17307, doi:10.1029/2004JD004759.

1. Introduction

[2] The global fleet of aircraft emits a range of trace species into the atmosphere, often directly into some of its cleanest regions. Aviation is also one of the fastest growing and least regulated sectors of the global economy. Of particular environmental importance are the emissions of carbon dioxide (CO_2), nitrogen oxides (NO and NO_2, collectively termed NO_x), and sulphur oxides (SO_2 and sulphate, collectively known as SO_x). In addition to the CO_2 released, aircraft and their emissions are a source of concern for several reasons, in particular, (1) the role of NO_x emissions from subsonic aircraft in the production of tropospheric ozone (O_3) and associated changes in the oxidizing capacity of the atmosphere [*Derwent et al.*, 1999; *Isaksen et al.*, 1999]; (2) the generation of contrails, and potential modification of cirrus clouds, linked to particle and water vapor emissions [*Fahey et al.*, 1999]; (3) changes in aerosol loading and heterogeneous chemistry, related to SO_x emissions [*Pitari et al.*, 2002]; and (4) the potential impact of pollution from future fleets of supersonic aircraft on the stratospheric ozone layer [*Isaksen et al.*, 1999]. All these processes generate changes in atmospheric composition that also have implications for radiative forcing of climate. Comprehensive discussions of these issues have been published in two major reports: the Intergovernmental Panel on Climate Change (IPCC) Special Report on Avia-

0148-0227/04/2004JD004759

tion [*Intergovernmental Panel on Climate Change* (*IPCC*), 1999]; and the European scientific assessment of the effect of aircraft emissions [*Brasseur et al.*, 1998].

[3] This paper focuses on the role of NO_x emissions from the current fleet of subsonic aircraft, and presents a modeling study of how these emissions impact on tropospheric O_3 and methane (CH_4). The impacts of aircraft SO_x emissions [e.g., *Pitari et al.*, 2002] are not included. Several previous studies [e.g., *Stevenson et al.*, 1997; *Isaksen et al.*, 1999] have shown that aircraft NO_x very efficiently generates tropospheric O_3, which exerts a positive radiative forcing [*Prather et al.*, 1999]. At the same time, increased levels of NO_x and O_3 lead to elevated levels of the hydroxyl radical (OH), the main determinant of the oxidizing capacity of the atmosphere, tending to reduce the atmospheric residence time of CH_4. This contributes an additional negative radiative forcing [*Prather et al.*, 1999]. *IPCC* [1999] considered that this negative CH_4 forcing had a relatively large uncertainty associated with it, as the mechanisms driving the changes in OH and hence CH_4 were poorly understood.

[4] To quantify the full climate impact of a trace gas emission, all radiative forcing effects must be integrated over their lifetimes [*Prather*, 2002]. This can best be achieved by introducing a pulse of trace gas emissions into a global model, and following the compositional perturbation generated by that pulse for a sufficiently long time period (i.e., several times the *e*-folding timescale of the longest-lived mode). For the tropospheric chemical system, *Prather* [1994] showed that the longest-lived time constant was determined by the perturbation lifetime (or adjustment time) of methane. The IPCC estimated the methane perturbation lifetime to be around 12 years [*Prather et al.*, 2001]. This indicates that the response of tropospheric chemistry needs to be integrated for a time period of the order of 100 years following an emission pulse, to fully quantify its climate impact. In practice, the model response has been found to settle down to a simple exponential decay after a few years, meaning that shorter model integrations can be used with simple extrapolation. Two recent studies [*Derwent et al.*, 2001; *Wild et al.*, 2001] have used this methodology to calculate the impact of aircraft NO_x upon both O_3 and CH_4, but neither of these presented detailed OH budgets. In this work, we present for the first time the impact of aircraft NO_x on modeled OH budgets, in order to explore the CH_4 forcing mechanism in detail. In addition, we also consider for the first time differences in the forcings arising from the season of the emission.

[5] In the following section, we introduce the climate-chemistry model used. In section 3 we describe the experiments performed. Section 4 presents results from these numerical experiments. Results from the control have been compared to observed ozonesonde data, and results from other models, in order to demonstrate the model's capability in simulating tropospheric O_3, OH and CH_4. Results from the aircraft perturbation experiments are discussed in terms of the radiative forcings associated with the resultant changes in O_3 and CH_4, in particular the magnitude and uncertainties surrounding these climate forcing mechanisms.

2. Climate-Chemistry Model Description

[6] The HadAM3-STOCHEM climate-chemistry model was used to carry out the series of numerical experiments. The chemistry submodel receives meteorological fields from the driving climate model, but chemical fields were not fed back into the radiation scheme of the climate model in the experiments described here. This allows us to perfectly isolate the chemical effects of aircraft emissions from any dynamical effects, as the dynamics remains unchanged in all the experiments. A fully coupled model would introduce significant noise, through minor perturbations to the dynamics that would make the aircraft signal very difficult to extract. The model version used was essentially the same as that described by *Sanderson et al.* [2003a, 2003b], although some of the boundary conditions and emissions differed slightly. A brief description of the main model components follows.

2.1. Climate Model: HadAM3

[7] The Hadley Centre atmosphere-only climate model (HadAM3 [*Pope et al.*, 2000]) is a general circulation model (GCM) describing the atmosphere, and forms the atmospheric component of the Hadley Centre coupled ocean-atmosphere climate model HadCM3 [*Johns et al.*, 2003]. The version of HadAM3 employed here used a prescribed sea surface temperature (SST) climatology (1978–1996) from AMIP II (Atmospheric Model Intercomparison Project II [*Taylor et al.*, 2000]) to provide the lower boundary condition over the oceans. Over land, the MOSES2.2 surface exchange scheme was used [*Essery et al.*, 2001] (see http://www.metoffice.com/research/hadleycentre/pubs/HCTN), together with a prescribed seasonal vegetation distribution. Surface characteristics are used to drive dry deposition and vegetation emissions of several species in the chemistry submodel STOCHEM [*Sanderson et al.*, 2003a, 2003b]. HadAM3 was run at standard climate resolution: 3.75° longitude × 2.5° latitude, with 19 vertical levels, concentrated toward the surface, but extending upward to ~10 hPa, with a vertical resolution in the upper troposphere/lower stratosphere (UT/LS) of about 50 hPa. The model time step was 30 min, with meteorological fields passed to STOCHEM every 3 hours.

2.2. Chemistry Submodel: STOCHEM

[8] STOCHEM is a Lagrangian tropospheric chemistry transport model, originally described by *Collins et al.* [1997], with subsequent major updates to chemistry [*Collins et al.*, 1999], convective mixing [*Collins et al.*, 2002], surface deposition [*Sanderson et al.*, 2003a], and vegetation emissions [*Sanderson et al.*, 2003b]. Brief descriptions of the main components are given below.

2.2.1. Transport and Mixing

[9] The STOCHEM model extends from the surface up to ~100 hPa. Within this domain, the atmosphere is divided into 50,000 equal mass air parcels, which are advected using winds from HadAM3, using a fourth-order Runge-Kutta method. For every 1 hour advection time step, winds are linearly interpolated to each parcel's position in the horizontal, and using cubic interpolation in the vertical. A random walk component is added to simulate horizontal and vertical diffusion. Following each advection step, air parcels are mapped to an Eulerian grid of dimensions 5° × 5° with nine equally spaced vertical levels, of thickness ~100 hPa. Each grid box contains, on average, two to three Lagrangian air parcels. This resolution is sufficient to crudely capture

Table 1. Global Annual Mean Emissions for 1990[a]

Trace Gas	Total	Anthropogenic	Biomass Burning	Vegetation	Soil	Ocean	Other Natural
NO	49.6	27.4 0.7[c] (aircraft)	8.2		5.6		7.3[b] (lightning) ~0.4[b] (stratosphere)
CO	1114	492	537	35		50	
CH_4	578	253	74	27[d] (termites)		13	211[e] (wetlands)
C_2H_6	14.9	9.6	4.1	1.2			
C_3H_8	13.0	11.3	1.2	0.5			
C_4H_{10}	81.9	78.8	1.9	1.2			
C_2H_4	22.3	10.7	8.5	3.1			
C_3H_6	22.9	12.7	8.5	1.7			
CH_3OH	11.2	6.5	4.7				
HCHO	1.7	1.0	0.7				
CH_3CHO	6.9	3.3	3.6				
Acetone	7.3	3.9	0.5	2.9			
O-xylene	16.4	15.1	1.3				
Toluene	24.2	16.2	8.0				
Isoprene	575			575[b]			
Terpene	191			191[b]			
H_2[f]	48	20	20		4.0	4.0	
SO_2	79.9	65.8	5.1				9.0 (volcanoes)
DMS	16				1.0	15.0	
NH_3[g]	53.6	39.4	3.5		2.5	8.2	

[a]Emissions are in Tg yr^{-1} (except NO and NH_3, which are in Tg(N) yr^{-1}, and SO_2 and DMS, which are in Tg(S) yr^{-1}). Unless otherwise indicated, anthropogenic, biomass-burning, and vegetation emissions are from IIASA (M. Amann et al., manuscript in preparation, 2004). The biomass-burning emissions have been doubled to bring them approximately in line with *IPCC* [2001] estimates for NO and CO.

[b]NO from lightning and the stratosphere (added as HNO_3) and isoprene and terpene from vegetation [*Sanderson et al.*, 2003b] are calculated interactively.

[c]Aircraft emissions are from *IPCC* [1999].

[d]CH_4 emissions from termites [*Sanderson*, 1996] utilize the vegetation emissions distribution.

[e]CH_4 emissions from wetlands use the distribution from *Aselmann and Crutzen* [1989] and have been scaled upward so that the modeled global CH_4 trend in the early 1990s approximately matches observations.

[f]H_2 emissions are from *Sanderson et al.* [2003a].

[g]NH_3 emissions are from EDGAR v2.0 [*Olivier et al.*, 1996].

the three-dimensional (3-D) global distribution of aircraft emissions, and is typical of global model studies to date [e.g., *Prather et al.*, 2001; *Wild et al.*, 2001]. To represent the deformation of air parcels, some interparcel mixing is implemented between air parcels within the same Eulerian grid volume. Air parcel concentrations are brought toward the mean value for the grid volume. Turbulent mixing in the boundary layer is achieved by randomly reassigning the vertical coordinates of air parcels over the depth of the layer. Convective mixing is described fully in *Collins et al.* [2002], and utilizes 3-D convective diagnostics from the climate model, including updraught and detrainment mass fluxes.

2.2.2. Emissions

[10] Global trace gas sources, by sector and species, are given in Table 1 for 1990. Anthropogenic (totals and distributions), biomass-burning (totals only) and vegetation (totals only) emissions are taken from the IIASA "business as usual" scenario (M. Amann et al., manuscript in preparation, 2004) for the years 1990 to 1995. Biomass-burning totals were doubled, to bring them approximately in line with *IPCC* [2001] estimates, whilst spatial and seasonal distributions were taken from *Cooke and Wilson* [1996]. Vegetation emissions of isoprene and terpene were distributed using spatial vegetation fields from the GCM land surface scheme, and for isoprene included a dependence upon temperature and photosynthetically available radiation [*Sanderson et al.*, 2003b]. Interactive lightning NO_x emissions (based on *Price et al.* [1997] and *Meijer et al.* [2001]) totaled ~7.3 Tg(N) yr^{-1}, with some interannual variability. Aircraft emissions were based on the NASA 1992 inventory [*Henderson et al.*, 1999], which shows some seasonality in both spatial distribution and the global total.

2.2.3. Chemistry

[11] The chemical scheme is as described by *Collins et al.* [1999], and includes 70 species that take part in 174 photochemical, gas phase, and aqueous phase reactions and equilibria. The mechanism describes the tropospheric chemistry of CH_4, CO (carbon monoxide), NO_x, O_3, and 11 nonmethane hydrocarbons (NMHC). All species are transported, as this incurs essentially no extra cost in the Lagrangian framework. The chemical time step is 5 min.

2.2.4. Deposition

[12] The updated dry deposition scheme is described in *Sanderson et al.* [2003a]. A soil sink for CH_4 is now included explicitly as a budget term, rather than reducing the global emissions, as was done in previous model versions [e.g., *Derwent et al.*, 2001]. Soil uptake of CH_4 is linked to model soil moisture [*Yonemura et al.*, 2000; *Reay et al.*, 2001]. The wet deposition scheme remains unchanged, and is described in detail by *Stevenson et al.* [2003].

2.2.5. Upper Boundary Conditions

[13] The top of the chemistry model is at ~100 hPa (~14 km), approximately at the level of the tropical tropopause, but extending well into the extratropical lower stratosphere. Most aircraft fly below this upper boundary, and emissions employed here are all below this level. To represent the influx of stratospheric O_3 to the model domain, we use vertical wind fields at this level, coupled with an ozone climatology [*Li and Shine*, 1995]. Similarly, we introduce an NO_y (total oxidized nitrogen) influx (as

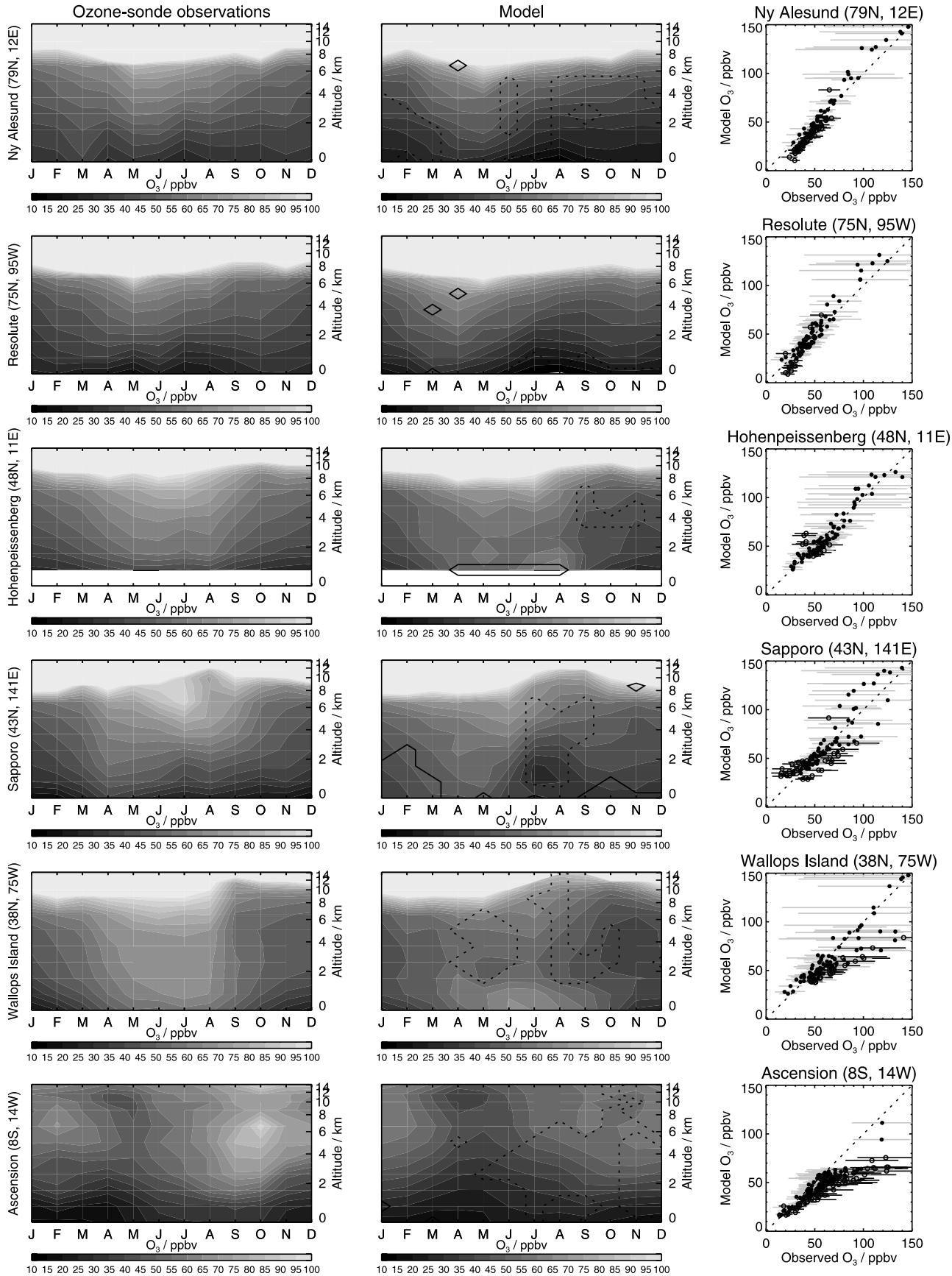
Ozone-sonde observations
Model
Ny Alesund (79N, 12E)
Resolute (75N, 95W)
Hohenpeissenberg (48N, 11E)
Sapporo (43N, 141E)
Wallops Island (38N, 75W)
Ascension (8S, 14W)
Altitude / km
J F M A M J J A S O N D
O3 / ppbv
10 15 20 25 30 35 40 45 50 55 60 65 70 75 80 85 90 95 100
Model O3 / ppbv
Observed O3 / ppbv

Figure 1

HNO_3), assuming a fixed mass ratio of N:O_3 of 1:1000 [*Murphy and Fahey*, 1994]. Above the model's tropopause, CH_4 is lost at a fixed rate, in order to simulate the small stratospheric methane sink [*Prather et al.*, 2001].

3. Experiments

[14] Five experiments were performed, each starting on 1 December 1988 and continuing through to the end of 1994. The first 13 months of each run were considered spin-up and were discarded, leaving 5 years of data (1990–1994) from each run for analysis. Since the atmospheric model is driven by climatological SSTs, the only connection between the model year and the real year is in the emissions fields. Results from the control simulation should therefore only be considered broadly representative of the early 1990s.

[15] The control simulation was followed by four sensitivity experiments, each of which differed from the control only in that aircraft NO_x emissions were increased by a factor of 10 for a single month (January, April, July or October) in 1990. Each experiment simulates the small differences in composition resulting from changes in emissions; the driving climate is identical in each case. For each experiment, monthly mean fields of the key model species and fluxes were output. Because the aircraft emissions inventory has some seasonal variation in total emissions, results from the aircraft pulse experiments require the application of small normalization factors in order to make them directly comparable. The extra aircraft emissions in each run totaled 1.194, 1.275, 1.368 and 1.292 Tg (NO_2) in each of the four months respectively. The results are normalized to 1 Tg(NO_2) in each case, assuming a linear dependence on emission; this assumption of linearity can reasonably be made given the rather small seasonal variation in aircraft emissions.

4. Results

4.1. Control Experiment

[16] Modeled ozone values (5 year means) from the control experiment are compared to climatological ozonesonde data [*Logan*, 1999; *Thompson et al.*, 2003a, 2003b] in Figure 1. The full seasonal cycle in the vertical profile of tropospheric O_3 (observed and modeled) is shown for six sites, from high northern latitudes to the tropics. The model profiles have been adjusted slightly, so that the upper tropospheric values are compared relative to the tropopause height (O_3 = 150 ppbv level), rather than absolute altitude, as in some cases the modeled tropopause height differs from observed. The third panel on each row directly compares modeled and observed ozone. The bars represent ±1 standard deviation in the observations. Solid (dashed) contours overlain on the modeled profiles indicate where the model overpredicts (underpredicts) the observations by more than one standard deviation. The points within these regions are plotted as red/blue in the direct data comparison. Figure 1 shows that the model captures the main features of the global cycle in tropospheric ozone in reasonable detail. Model deficiencies include some underestimation of mid- to lower-tropospheric O_3 at high northern latitudes, and an underestimation of mid- to upper-tropospheric O_3 at middle and especially low latitudes during Northern Hemisphere summer and autumn. These comparisons should be viewed with some caution, as it is difficult to directly compare individual stations with output from a relatively course (spatial resolution $5^\circ \times 5^\circ$) model driven by a GCM climate.

[17] Table 2 gives a global budget analysis for tropospheric ozone from the control experiment, averaged over 1990–1994. The ozone budgets are reported for three slightly different regions of the model domain, all of which have been used in earlier studies [e.g., *Collins et al.*, 2000; *Prather et al.*, 2001]. Our preferred definition of the troposphere is where monthly mean ozone is less than 150 ppbv, and this was mainly used for the IPCC Third Assessment Report (TAR) budgets [*Prather et al.*, 2001]. Using other definitions has relatively minor impacts on individual absolute budget terms, but strongly influences net chemical production, inferred net stratospheric input, O_3 burden and lifetime (see Table 2). STOCHEM contains a comparatively large amount of nonmethane hydrocarbon chemistry, and total O_3 production and loss terms are slightly higher than IPCC TAR values – this may also reflect other differences (e.g., higher isoprene emissions). This also causes the mean tropospheric O_3 lifetime ($\sim$19 days) to be slightly below the IPCC TAR range. Net stratospheric input of $\sim$400 Tg(O_3) yr^{-1} is toward the lower end of the range of other models, but the O_3 burden is in the middle of the range.

[18] Table 3 presents the global methane budget for the control experiment (averaged over 1990–1994), over the whole model domain. All the budget terms are comparable to IPCC TAR values, although the minor soil sink term is double the IPCC estimate. *Smith et al.* [2000] estimated that the range for the soil sink is 7 to >100 Tg(CH_4) yr^{-1}, a wider range than suggested by IPCC TAR (30 ± 15 Tg(CH_4) yr^{-1}). Our relatively high value (61 Tg(CH_4) yr^{-1}) is well within the *Smith et al.* [2000] range. Wetland methane emissions (the largest and most uncertain natural source) were adjusted so that the model approximately generated the observed trend in global CH_4 for the early 1990s. In the current model version, wetland CH_4 emissions are not linked interactively with climate. Modelled CH_4 lifetimes (Table 3) are marginally shorter than IPCC esti-

Figure 1. Comparison of O_3 from the control experiment with ozonesonde observations at six sites. The first column shows observations from *Logan* [1999] and *Thompson et al.* [2003a, 2003b]. The second column is the equivalent plot from the model, with a minor adjustment made to the vertical coordinate so that the height of the O_3 = 150 ppbv contour in the model is aligned with the same contour in the observations. This accounts for any mismatch between the modeled and observed tropopause height. The final column compares all points, with bars indicating the standard deviation in the observations. Where the model overpredicts (underpredicts) observations by more than one standard deviation, the point is plotted with an open symbol in red (blue); these points are shown in the second column by the solid (dashed) contours. See color version of this figure at back of this issue.

Table 2. Global "Tropospheric" Ozone Budget From the Control Experiment (Mean of 1990–1994) for Three Slightly Different Model Regions and the Range of Model Results Reported by Intergovernmental Panel on Climate Change (IPCC) Third Assessment Report (TAR)[a]

Budget Term	Troposphere[b]	Surface to 100 hPa	Surface to 250 hPa	IPCC TAR
HO_2 + NO	3393	3431	3042	
CH_3O_2 + NO	876	880	837	
RO_2 + NO	706	708	682	
Total chemical production	4975	5019	4561	2334–4320
$O(^1D)$ + H_2O	2355	2357	2346	
O_3 + HO_2	1224	1263	1189	
O_3 + OH	485	513	458	
O_3 + hydrocarbons	126	126	126	
Other chemical loss	231	232	227	
Total chemical loss	4421	4491	4346	2511–4065
Net chemical production	+554	+528	+215	−810 to +507
O_3 dry deposition	949	949	949	533–1178
Net stratospheric input[c]	+395	+421	+734	391–1440
O_3 burden ($Tg(O_3)$)	273	390	220	193–370
O_3 lifetime (days)	18.6	26.2	15.2	20.7–26.4

[a]Fluxes are in $Tg(O_3)$ yr^{-1}.
[b]The troposphere is defined as where the monthly mean O_3 (averaged over the 5 year control run) is less than 150 ppbv.
[c]Net stratospheric input is calculated as the residual of other budget terms.

mates, but well within the range of uncertainty, indicating that the model's OH distribution is consistent with our best estimates of the global atmospheric oxidizing capacity.

[19] This brief analysis of the control experiment indicates that the model can simulate the main characteristics of the global O_3, CH_4 and OH distributions and global budgets. We now explore the model's response to perturbations in aircraft NO_x emissions.

4.2. Aircraft Pulse Experiments

4.2.1. Globally Integrated Perturbations

[20] Figure 2 shows how the global model burdens (the atmospheric mass of a species, integrated over the whole model domain) of several key components are perturbed relative to the control, for each aircraft pulse experiment. The global NO_x burden (Figure 2a) increases during the month of emission by 60–110 $Gg(NO_2)$, but the positive anomaly rapidly dissipates, reflecting the short atmospheric lifetime of NO_x (typically a few days). Because the majority of aircraft NO_x emissions are located in northern midlatitudes, the July pulse experiences summer conditions (higher OH levels), and hence a shorter NO_x lifetime, and generates a smaller NO_x burden anomaly. The October, and to a lesser extent January, pulses generate small negative NO_x burden anomalies after ~2 months – these stem from wintertime titration effects associated with the extra O_3 produced by the initial NO_x increase.

[21] Ozone burden anomalies (Figure 2b) peak either during or in the month after the emission pulse, then decay at a rate reflecting the O_3 lifetime of typically a few weeks (again, shorter during summer). After ~6–8 months, the O_3 anomaly becomes slightly negative, reflecting the lowering of CH_4 (see below) and CO, both important O_3 precursors.

[22] The additional NO_x generates a pulse of OH for 1–2 months (Figure 2c), due to increases in both NO and O_3. The OH anomaly is determined by perturbations to a large number of reactions that both produce and destroy OH. Figure 3 shows the impact of the January pulse on the global OH budget, during and immediately following the pulse. The main source of extra OH is the reaction

$$NO + HO_2 \rightarrow NO_2 + OH; \quad (1)$$

this predominates during the first month. This source rapidly declines following the pulse, due to the short NO_x lifetime, eventually becoming an OH sink as the NO_x anomaly turns negative, due to O_3 titration effects (see above). The second most important reaction, which becomes the dominant extra OH source in the second month, is

$$O(^1D) + H_2O \rightarrow 2OH; \quad (2)$$

Table 3. Global Methane Budget and Lifetimes With Respect to the Various Sink Processes for the Control Experiment and Compared With IPCC TAR[a]

Budget Term	Control 1990–1994	IPCC TAR	Perturbation ΔCH_4	IPCC TAR ΔCH_4
CH_4 total emission	588	598		
CH_4 + OH	485	506		
CH_4 dry deposition	61	30		
CH_4 stratospheric loss	21	40		
Trend	+21 (7.6 ppbv yr^{-1})	+22 (7.9 ppbv yr^{-1})		
CH_4 lifetime (OH), years	9.4	9.6	13.9	14.5
CH_4 lifetime (soils), years	74	160		
CH_4 lifetime (stratosphere), years	214	120		
CH_4 lifetime (total), years	8.0	8.4	11.1	12.0

[a]The mean CH_4 perturbation lifetime (averaged across the four sensitivity experiments) and the equivalent IPCC TAR values are also given. The methane budget is in $Tg(CH_4)$ yr^{-1} over the whole model domain (surface to 100 hPa).

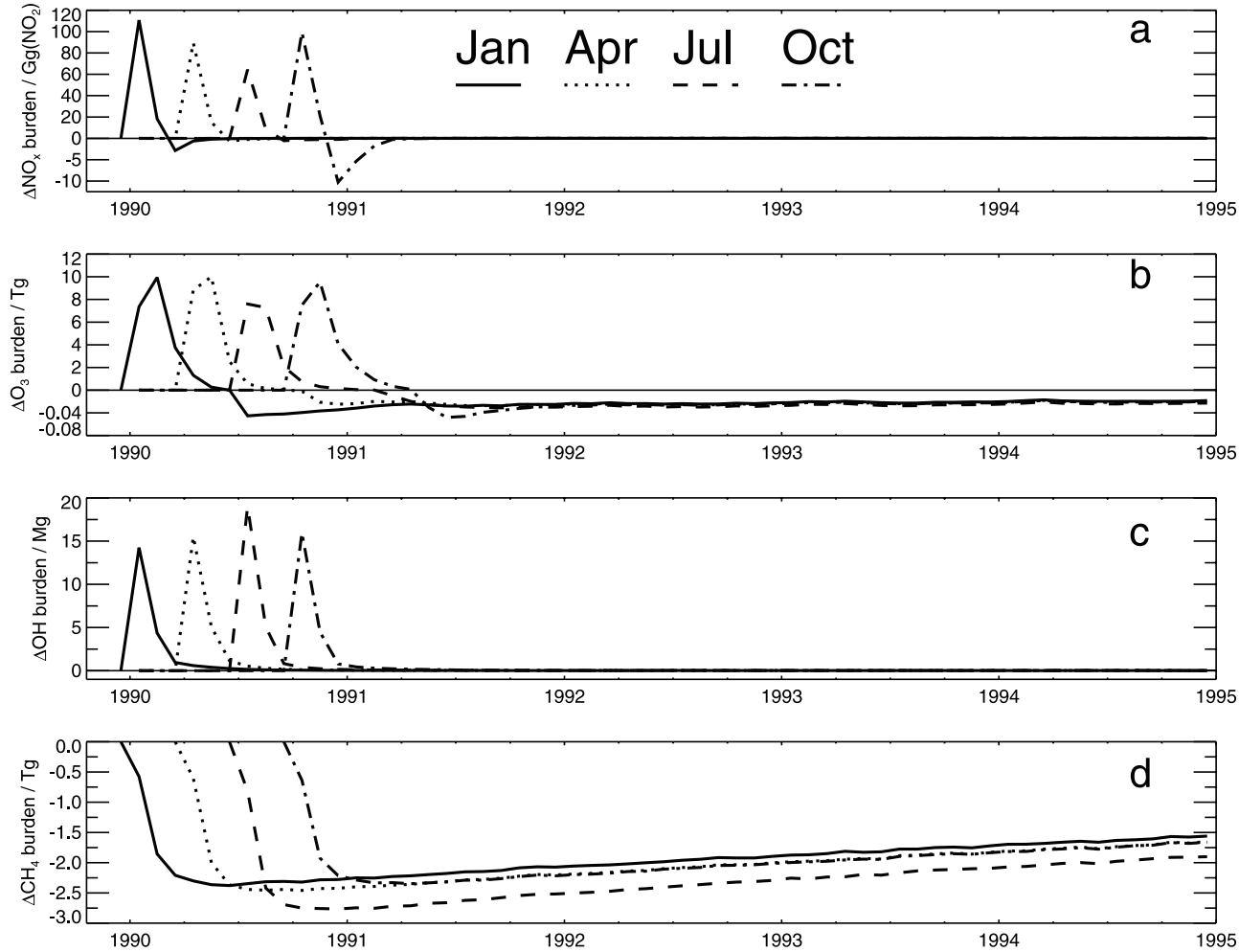

Figure 2. Time evolution of perturbations (relative to the control experiment) in the global burdens of (a) NO_x, (b) O_3, (c) OH, and (d) CH_4 for the four aircraft NO_x experiments (pulses emitted in January (solid red lines), April (dotted green lines), July (dashed dark blue lines), and October (dash-dotted light blue lines)). Note that the negative scales for NO_x and O_3 have been expanded for clarity. See color version of this figure in the HTML.

this is driven upward by the rise in O_3. The only other significant OH source term is also related to O_3:

$$O_3 + HO_2 \rightarrow OH + 2O_2. \quad (3)$$

The two most important OH sink reactions that rise in response to elevated OH are

$$CO + OH(+O_2) \rightarrow CO_2 + HO_2 \quad (4)$$

and

$$CH_4 + OH(+O_2) \rightarrow CH_3O_2 + H_2O. \quad (5)$$

By the March following the January pulse, the main extra OH source term is due to a reduced flux though the sink reaction (4), driven by the reduction in CO built up over the first two months.

[23] The enhanced CH_4 oxidation flux (reaction (5)) results in a global depletion of CH_4 (Figure 2d), that accumulates over the first 5–6 months, mainly occurring in the first two months. The reduction of CH_4 also causes reaction (5) to switch over to become an OH source after six months, through a similar mechanism to reaction (4). Reaction (4) responds more quickly because of CO's shorter lifetime. The peak magnitude of the CH_4 anomaly reflects the size of the OH pulse, and is largest in July (-2.8 Tg(CH_4)) and smallest in January (-2.4 Tg(CH_4)). The CH_4 perturbations then all decay with roughly the same *e*-folding lifetime of 11.1 years (Tables 3 and 4), 39% longer than the overall CH_4 lifetime in the control run (8.0 years, see Table 3), in reasonable agreement with earlier estimates of the perturbation lifetime (12 years) [*Prather et al.*, 2001]. These OH budget perturbations have important spatial distributions, which are explored in the next section.

4.2.2. Zonal Mean Perturbations

[24] Figure 4 shows monthly mean, zonal mean perturbations for NO_x, O_3 and OH for the January aircraft pulse experiment, relative to the control, over the 3 months during and following the pulse. In the plots, filled contours represent increases and open contours show decreases. Broadly similar features occur for the experiments in other seasons. The initial NO_x anomaly mirrors the aircraft

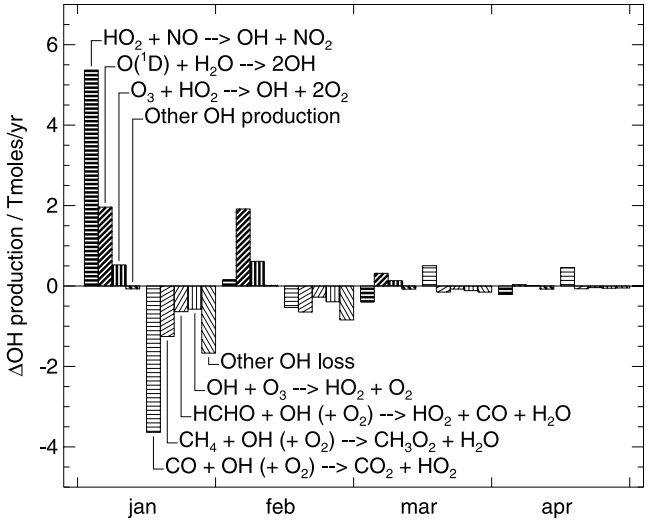

Figure 3. Impact of the January emissions pulse on the global OH budget for January–April. For each month the first four bars show perturbations to the OH production fluxes (reactions (1)–(3), together with the sum of other minor OH production reactions). The other five bars show perturbations to the OH loss fluxes (reactions (4) and (5), then many progressively less important reactions). Note that a reduction in an OH production flux represents an OH sink (e.g., reaction (1) in March and April) and vice versa: a reduction in an OH destruction flux represents an OH source (e.g., reaction (4) in March and April). Emissions pulses in other months display similar responses. See color version of this figure in the HTML.

emissions distribution, with only limited transport and mixing away from the source regions. The extra NO_x drives ozone production, generating the O_3 anomaly. This anomaly initially resembles the NO_x anomaly, but is weighted toward the surface (where the chemistry proceeds more rapidly) and the Southern Hemisphere (where the cleaner background increases the ozone production sensitivity to NO_x), and displays more transport and mixing, due to the longer O_3 lifetime. The O_3 anomaly grows in the second month, before starting to decay in the third month, most rapidly in the tropics, where the O_3 lifetime is shortest, and most slowly in the high-latitude UT/LS, where the lifetime is longest. The NO_x anomaly rapidly decays, also most slowly in the UT/LS, where its lifetime is longest. In the lower troposphere, a negative NO_x anomaly develops, due to the increased levels of O_3 and OH. The OH anomaly is initially mainly driven by the extra NO_x, but after the emission pulse month, the extra O_3 becomes the major OH source (Figure 3). The vertical and latitudinal shape of the OH anomaly is important in determining its impact on CH_4, because methane oxidation increases strongly with temperature, mostly occurring toward the surface in the tropics.

[25] To understand the mechanisms responsible for the OH anomaly, it is useful to look at the spatial and temporal structure of the main perturbations to the OH budget in more detail (Figure 5). This figure shows monthly zonal mean plots of the main perturbations to OH production and loss fluxes, for the same three months as Figure 4, and for the main reactions in Figure 3. The first three rows of Figure 5 display perturbations to OH production fluxes (reactions (1), (2), and (3)), whilst the last two rows show perturbations to OH loss fluxes (reactions (4) and (5)). The loss fluxes are multiplied by minus one, so that all positive values (filled contours) in Figure 5 represent enhanced OH sources, whereas all negative values (open contours) show enhanced OH sinks. Reaction (1) (1st row of Figure 5) mainly reflects changes in NO_x (1st row of Figure 4). Reactions (2) and (3) (2nd and 3rd rows of Figure 5) are largely controlled by the extra O_3 (2nd row of Figure 4),

Table 4. Characteristics of the CH_4 and O_3 Perturbations and Their Associated Radiative Forcings (Including Stratospheric Adjustment and Normalized for a 1 Tg(NO_2) Emission Pulse)[a]

	ΔCH_4		ΔO_3 (Short Term)		ΔO_3 (Long Term)		Net	
Emission Pulse	*e*-Fold, years	Total, ppbv-yr	RF, mW m^{-2} yr	Total, ppbv-yr	RF, mW m^{-2} yr	Total, ppbv-yr	RF, mW m^{-2} yr	RF, mW m^{-2} yr
January	11.13	−10.32	−3.83	0.24	4.61	−0.041	−0.90	−0.11
April	11.05	−10.82	−4.00	0.23	5.30	−0.041	−0.89	+0.41
July	11.09	−11.92	−4.42	0.19	5.14	−0.046	−0.99	−0.26
October	10.99	−10.23	−3.76	0.26	5.17	−0.040	−0.89	+0.50
Mean	11.07	−10.82	−4.00	0.23	5.06	−0.042	−0.92	+0.14
Lifetime corrected[b]	11.53	−11.3	−4.2	0.23	5.06	−0.044	−0.95	−0.09
Wild (year)	14.2	−14.7	−5.5	0.36	11.5	−0.081	−2.6	+3.4
Lifetime/O_3 corrected[b,c]	11.8[b]	−12.2[b]	−4.6[b]	0.36	7.9[e]	−0.067[b]	−1.5[b,c]	+1.8
Derwent (January)	12.3	−15.9	−6.9	0.52	36.0[d]	...	...	+29
Reworked	12.3	−14.8	−5.5[e]	0.40	10.9[e]	−0.04[f]	−1.4[f]	+4.0
Lifetime/O_3 corrected[b,c]	10.4[b]	−12.5[b]	−4.6[b,d]	0.40	8.6[c,e]	−0.03[b,f]	−0.7[b,c,f]	+3.3

[a]The O_3 perturbation is split into the initial (short-term) positive phase and the (long-term) negative phase. Results are compared with *Wild et al.* [2001] and our earlier work [*Derwent et al.*, 2001].

[b]The "lifetime-corrected" rows have been adjusted assuming values for the CH_4 soil and stratospheric sinks as reported by *Prather et al.* [2001]. For this work the IPCC lifetimes have been substituted for the model-derived values; *Wild et al.* [2001] and *Derwent et al.* [2001] only used the OH-derived lifetime.

[c]The *Wild et al.* [2001] and *Derwent et al.* [2001] O_3 forcings have been recalculated using the annual mean value from this study of 22 mW m^{-2} $ppbv^{-1}$.

[d]*Derwent et al.* [2001] calculated CH_4 forcings using a value of 0.43 mW m^{-2} $ppbv^{-1}$, rather than the value of 0.37 mW m^{-2} $ppbv^{-1}$ used in this study; the latter value is used for the reworked values.

[e]*Derwent et al.* [2001] mistakenly reported O_3 forcings normalized to 1 Tg(N) rather than 1 Tg(NO_2): the originally reported values need reducing by a factor of (46/14).

[f]Values for the negative phase of the O_3 anomaly were not reported by *Derwent et al.* [2001]; these values are estimates.

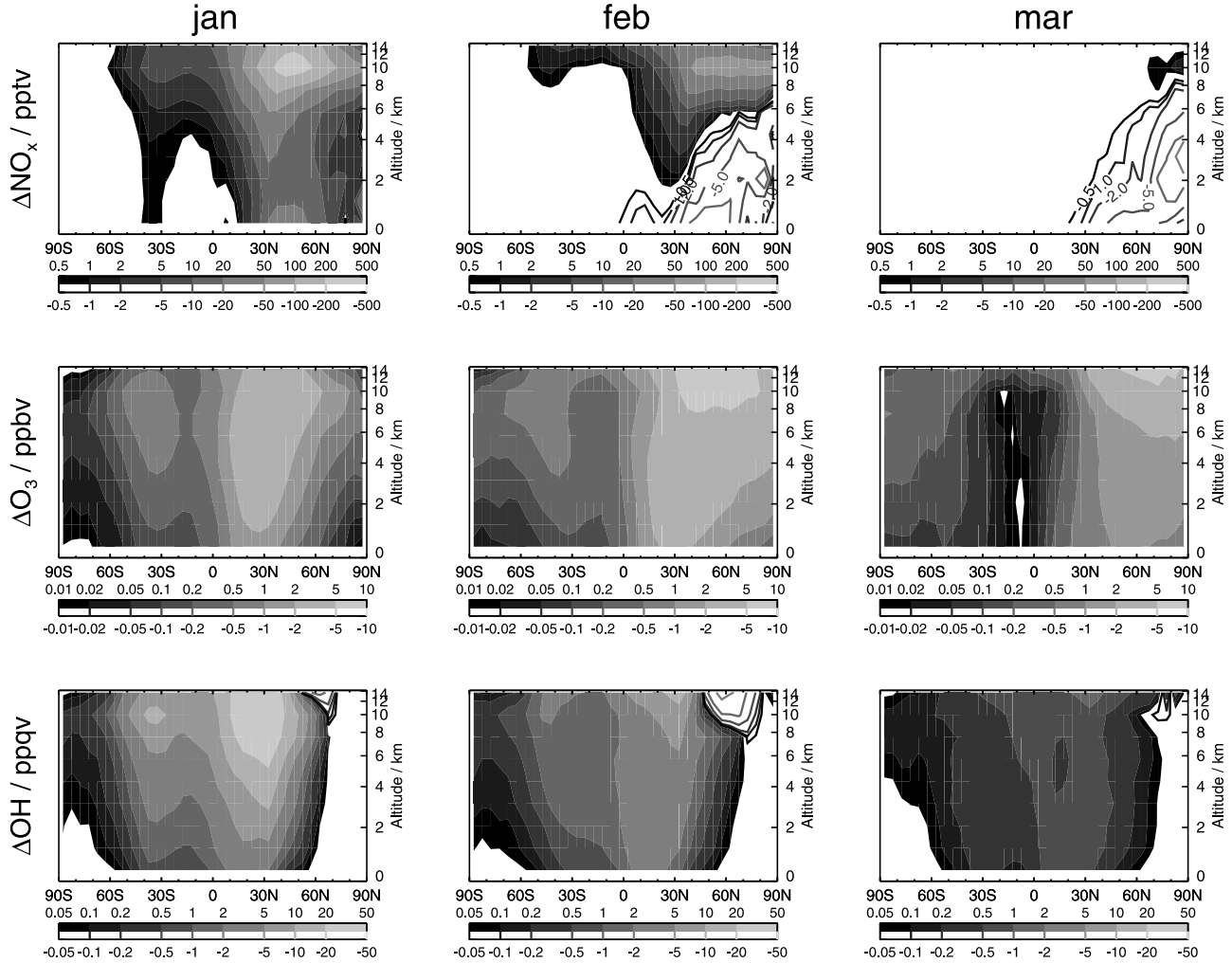

Figure 4. Monthly mean, zonal mean perturbations to (top) NO_x (pptv), (middle) O_3 (ppbv), and (bottom) OH (ppqv (parts per 10^{15} by volume)) in (left) January, (center) February, and (right) March for the January aircraft emissions pulse experiment. Filled contours show increases, and open contours show decreases. Emissions pulses in other months display similar responses. See color version of this figure at back of this issue.

although reaction (3) is also affected by changes in HO_2 via reaction (1) in the UT/LS. The methane oxidation flux perturbation distribution is very important, as this illustrates where the methane loss occurs – predominantly in the midtroposphere at 10°–30°N during the first month, and at 0°–30°N in the lower troposphere subsequently. The source of the OH driving the enhanced CH_4 oxidation comes from a combination of reactions (1) and (2) initially, then from reactions (2) and (3). This illustrates that the source of OH arising through the O_3 route is important in determining the CH_4 perturbation, as O_3 transport and mixing represents a mechanism for transporting the aircraft impact from the midlatitude UT to the tropical lower troposphere. Similar behavior is seen for the aircraft pulses in other seasons. *Isaksen et al.* [1999] suggested that CO could play an important role in spreading the aircraft impact, but we find that perturbations to CO oxidation (reaction (4)) act mainly to reduce OH, and thus cannot contribute to the enhanced CH_4 oxidation. Only in the third (and subsequent) months (Figure 3) does the perturbation to CO oxidation become an OH source, but by this time most of the CH_4 anomaly has already been generated.

4.3. Radiative Forcing Calculations

[26] To estimate the overall climate forcing from aircraft NO_x emissions, time-integrated radiative forcings were calculated for the ozone and methane perturbations, over a 100 year time horizon [e.g., *Derwent et al.*, 2001; *Wild et al.*, 2001]. For methane, because the perturbation is long-lived it becomes well mixed throughout the atmosphere, so the radiative forcing calculation is relatively straightforward. For ozone, the perturbation has two stages (Figure 2b): a short-lived (~6 months) positive phase (with a distinct spatial structure: Figure 4), followed by a long-lived (and hence more geographically homogeneous) negative phase, associated with (and decaying at the same rate as) the negative CH_4 anomaly. Because the numerical experiments were only continued for 4–5 years after the emissions pulses, the anomalies need to be extrapolated out to 100 years. As

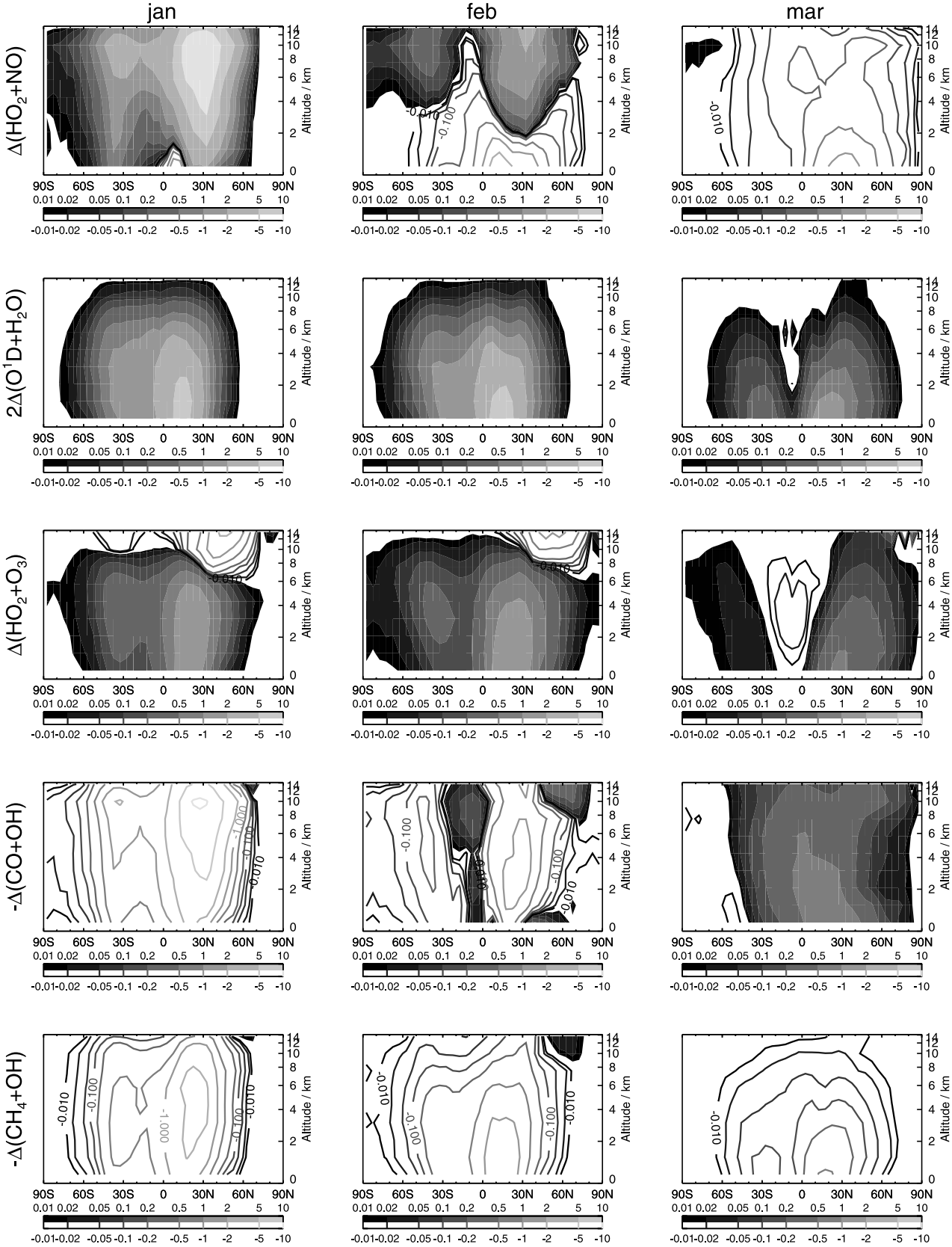

Figure 5. Monthly zonal mean perturbations to the major OH production and loss fluxes (ppbv/month) for the three months during/following the January emissions pulse. The two lowest rows show perturbations to OH loss reactions (4) and (5) and are multiplied by −1. Hence filled contours represent OH production, and open contours represent OH destruction. Emissions pulses in other months display similar responses. See color version of this figure at back of this issue.

already noted, the CH_4 perturbation decays with an *e*-folding timescale of ~11.1 years (Table 4). The long-lived component of the O_3 perturbation decays at the same rate, as it is also being generated by the CH_4 anomaly. This timescale is used to extrapolate the CH_4 and O_3 anomalies.

[27] Integrated CH_4 anomalies (ppbv-yr) for each experiment are given in Table 4; these are converted to radiative forcings by assuming a simple relationship between forcing and change in concentration of 0.37 mW m^{-2} $ppbv^{-1}$ [*Schimel et al.*, 1996]. The largest magnitude forcing arises for the July emissions pulse, which is ~17% larger than the CH_4 forcing for the October pulse (Figure 2d, Table 4). The mean response for the four months is also given, and this can be compared to the results of *Wild et al.* [2001], who conducted a similar experiment, but with a yearlong emissions pulse. The main difference is in the perturbation *e*-folding time, which is ~28% longer in the *Wild et al.* [2001] study (14.2 years), partly because this study did not explicitly include methane sinks for soils and the stratosphere. Neglect of these sinks produces a proportionately larger forcing. After accounting for this, our results are in quite close agreement with *Wild et al.* [2001]. Compared to our earlier work [*Derwent et al.*, 2001], the CH_4 results are about one third smaller, and this can only be partially explained by a shorter perturbation *e*-folding timescale. See section 5 for other possible explanations.

[28] Table 4 also gives integrated O_3 anomalies (ppbv-yr) for both the initial positive (~first 6 months) and long-term negative phases of the O_3 perturbation (Figure 2b). These O_3 anomalies have been converted to radiative forcings using an off-line radiation code [*Edwards and Slingo*, 1996], following the methods described by *Stevenson et al.* [1998]. Full account is taken of stratospheric temperature adjustment, which tends to reduce instantaneous forcings by ~22%. The initial positive forcing is largest for the April emissions pulse, and least for the January pulse. This represents a complex tradeoff between net O_3 production chemistry (highest in April), O_3 lifetime (longest in January), and forcing per O_3 molecule (highest in July). The integrated long-term negative forcing is ~17–20% of the short-term positive forcing. The results are again similar to the study of *Wild et al.* [2001], although the ozone response is slightly less, even after accounting for the shorter perturbation lifetime. *Wild et al.* [2001] used a fixed factor to convert between ozone concentrations and radiative forcings, rather than a full radiation calculation as performed here. We find a conversion factor of 19 mW m^{-2} $ppbv^{-1}$ (for the January pulse), rising to 27 mW m^{-2} $ppbv^{-1}$ (for the July pulse); these compare to a value of 32 mW m^{-2} $ppbv^{-1}$ used by *Wild et al.* [2001]. Our O_3 forcings are consequently smaller. Results for O_3 from our earlier work [*Derwent et al.*, 2001], suggest an O_3 anomaly roughly double the size, and a forcing 8 times larger (comparing with our January results). This study incorrectly normalized results (using 1 Tg(NO_2) rather than the reported 1 Tg(N)) consequently introducing an error of 46/14. The study also neglected the long-term negative component. After accounting for these two factors, our new work is in approximate agreement.

[29] We find that net forcings (adding the effects of O_3 and CH_4) are close to zero (monthly values of −0.26 mW m^{-2} yr to +0.50 mW m^{-2} yr, see Table 4). If our more accurate method for calculating the O_3 forcing from the O_3 anomaly is followed for the *Wild et al.* [2001] results, and their perturbation lifetime reduced, their net positive forcing of +3.4 mW m^{-2} yr is reduced to +1.8 mW m^{-2} yr, more closely in line with our results. Similarly, reworking of the *Derwent et al.* [2001] results produces a small positive net forcing of +3.3 mW m^{-2} yr. These forcings are global mean values – there are of course potentially significant nonzero local forcings.

5. Discussion

5.1. Is the Size of the Pulse Important?

[30] The use of a 10-fold increase in monthly aircraft emissions as the pulse size was to produce a large signal in the model, but also to remain within reasonably realistic bounds for atmospheric concentrations of NO_x. *Derwent et al.* [2001] used a smaller pulse (~1.5 times monthly aircraft emissions), and *Wild et al.* [2001] used an even smaller pulse (~0.7 times), but with a year's duration. Owing to nonlinearity in the response of O_3 to NO_x, different pulse sizes might be expected to yield different results, with the O_3 response saturating at higher NO_x levels. There may be some evidence of this in our results, which show slightly less of an ozone anomaly compared to the previous work (Table 4). It is mainly the size of this initial positive ozone anomaly that determines the sign and magnitude of the overall net forcing. Further work, considering a range of pulse sizes, is required to fully test this hypothesis, but we should introduce a note of caution when considering the results presented here, especially in absolute radiative forcing terms.

5.2. Is the Season of the Pulse Important?

[31] Our results show a complex tradeoff between the seasonal response of O_3 and OH to the NO_x pulses. The largest initial O_3 anomaly is for the October pulse, mainly a consequence of the longer lifetime in the following months (Figure 2b). Conversely, the smallest initial O_3 response is for the July pulse, when the lifetime is shortest. However, in terms of radiative forcing generated by the O_3 anomaly, the largest response is for April, and the smallest for January (Table 4).

[32] The OH anomalies, which go on to generate the CH_4 anomalies, depend on several factors, including the NO_x and O_3 anomalies, but also the availability of sunlight, which appears overriding, generating a peak response in July, and a minimum in January (Figure 2c). These translate into a maximum CH_4 anomaly in July, and a minimum in October (but very similar in January).

[33] The magnitudes of the positive and negative forcing anomalies are very similar, leading to a net forcing of near zero, but with a complex seasonal structure (positive in April and October, negative in January and July), and with a maximum difference between seasons of about 0.8 mW m^{-2} yr. Further calculations for intervening months may well reveal an even more complex seasonal structure to both the ozone and OH responses.

5.3. How Model-Dependent Are the Results?

[34] Broad agreement between this study and the earlier results of *Wild et al.* [2001] and our results from a previous version of the model [*Derwent et al.*, 2001] are encourag-

ing. However, it is clear that the climate forcings are controlled by the chemical and transport schemes within the models. In particular, the ozone chemistry in the upper troposphere, and its sensitivity to NO_x, is crucial. The persistence of the initial ozone anomaly relies on the correct ozone lifetime in the model. Large-scale and convective transport of ozone are important in the generation of the OH anomaly, and hence the CH_4 anomaly. Mixing and convective transport in models have large associated uncertainties [e.g., *Collins et al.*, 2002; *Lawrence et al.*, 2003]. Finally, the perturbation lifetime of CH_4 is also uncertain by about ±10% [*Prather et al.*, 2001], and this directly influences the magnitudes of both the methane and the long-term negative ozone anomalies. Further experiments within a variety of differently formulated models are required to confirm our results quantitatively.

6. Conclusions

[35] A chemistry-climate model has been used to investigate the radiative forcings generated by aircraft NO_x emissions. Results from a control experiment indicate that the model can represent tropospheric ozone, methane and OH in the present-day atmosphere reasonably well. Four further sensitivity experiments, releasing an extra pulse of aircraft NO_x emissions over a single month (January, April, July, and October), allow us to track the impacts of the emissions on the global atmospheric composition, and compare seasonal differences. The extra NO_x produces ozone in the upper troposphere; this ozone generates a positive radiative forcing, and with a lifetime of a few weeks, transfers the effects of aircraft away from the flight lanes, via convection and large-scale transport. The extra NO_x and O_3 perturb the OH budget, tending to increase OH levels. In turn, this extra OH increases methane destruction, and generates a negative CH_4 anomaly. This methane anomaly decays with a characteristic lifetime of 11.1 years (the perturbation lifetime), in reasonable agreement with IPCC estimates [*Prather et al.*, 2001]. This long-lived mode becomes dominant after the initial NO_x and positive O_3 anomalies have subsided (~6 months), and generates a negative climate forcing, mainly via CH_4, but with an additional component from an associated negative O_3 anomaly. We find that the integrated negative radiative forcing from the long-lived mode approximately balances the short-term positive forcing from the initial O_3 anomaly. Previous work [*Derwent et al.*, 2001; *Wild et al.*, 2001] suggests a small net positive forcing. Our less positive net forcing may reflect the larger emission pulses used in this work, and the nonlinearity of the ozone response to extra NO_x. The results suggest significant seasonal differences in the responses of the atmospheric composition to aircraft NO_x. The magnitude and structure of both the initial ozone and subsequent methane and ozone perturbations is strongly controlled by the representation of chemistry, transport and mixing in the model. Further work with a variety of different models is required to increase our confidence in these results.

[36] **Acknowledgments.** D.S.S. thanks the Environment Agency and Natural Environment Research Council for fellowship funding (P4-F02, NER/J/S/2000/00840). R.M.D. thanks NERC for UTLS-O_3 funding (NER/T/S/2000/01041). M.J.S., W.J.C., and C.E.J. acknowledge funding from the Government Meteorological Research program and from DEFRA through contract CPEA7.

References

Aselmann, I., and P. Crutzen (1989), Global distribution of natural freshwater wetlands and rice paddies, their net primary productivity, seasonality, and possible methane emissions, *J. Atmos. Chem.*, *8*(4), 307–358.

Brasseur, G., R. Cox, D. Hauglustaine, I. Isaksen, J. Lelieveld, D. Lister, R. Sausen, U. Schumann, A. Wahner, and P. Wiesen (1998), European scientific assessment of the atmospheric effect of aircraft emissions, *Atmos. Environ.*, *32*, 2329–2418.

Collins, W. J., D. S. Stevenson, C. E. Johnson, and R. G. Derwent (1997), Tropospheric ozone in a global-scale three-dimensional Lagrangian model and its response to NO_x emission controls, *J. Atmos. Chem.*, *26*, 223–274.

Collins, W. J., D. S. Stevenson, C. E. Johnson, and R. G. Derwent (1999), Role of convection in determining the budget of odd hydrogen in the upper troposphere, *J. Geophys. Res.*, *104*, 26,927–26,941.

Collins, W. J., D. S. Stevenson, C. E. Johnson, and R. G. Derwent (2000), The European regional ozone distribution and its links with the global scale for the years 1992 and 2015, *Atmos. Environ.*, *34*, 255–267.

Collins, W. J., R. G. Derwent, C. E. Johnson, and D. S. Stevenson (2002), A comparison of two schemes for the convective transport of chemical species in a Lagrangian global chemistry model, *Q. J. R. Meteorol. Soc.*, *128*, 991–1009.

Cooke, W. F., and J. J. N. Wilson (1996), A global black carbon aerosol model, *J. Geophys. Res.*, *101*, 19,395–19,409.

Derwent, R., et al. (1999), Impacts of aircraft emissions on atmospheric ozone, in *IPCC Special Report on Aviation and the Global Atmosphere*, edited by J. E. Penner et al., pp. 29–64, Cambridge Univ. Press, New York.

Derwent, R. G., W. J. Collins, C. E. Johnson, and D. S. Stevenson (2001), Transient behaviour of tropospheric ozone precursors in a global 3-D CTM and their indirect greenhouse effects, *Clim. Change*, *49*, 463–487.

Edwards, J. M., and A. Slingo (1996), Studies with a flexible new radiation code. I: Choosing a configuration for a large-scale model, *Q. J. R. Meteorol. Soc.*, *122*, 689–719.

Essery, R., M. Best, and P. Cox (2001), MOSES2. 2. Technical documentation, *Hadley Centre Tech. Note 30*, Met Office, Bracknell, U. K.

Fahey, D. W., et al. (1999), Aviation-produced aerosols and cloudiness, in *IPCC Special Report on Aviation and the Global Atmosphere*, edited by J. E. Penner et al., pp. 65–120, Cambridge Univ. Press, New York.

Henderson, S. C., et al. (1999), Aircraft emissions: Current inventories and future scenarios, in *IPCC Special Report on Aviation and the Global Atmosphere*, edited by J. E. Penner et al., pp. 290–331, Cambridge Univ. Press, New York.

Intergovernmental Panel on Climate Change (IPCC) (1999), *IPCC Special Report on Aviation and the Global Atmosphere*, edited by J. E. Penner et al., 373 pp., Cambridge Univ. Press, New York.

Intergovernmental Panel on Climate Change (IPCC) (2001), *Climate Change 2001: The Scientific Basis*, edited by J. T. Houghton et al., 881 pp., Cambridge Univ. Press, New York.

Isaksen, I., et al. (1999), Modelling the chemical composition of the future atmosphere, in *IPCC Special Report on Aviation and the Global Atmosphere*, edited by J. E. Penner et al., pp. 121–163, Cambridge Univ. Press, New York.

Johns, T. C., et al. (2003), Anthropogenic climate change for 1860 to 2100 simulated with the HadCM3 model under updated emissions scenarios, *Clim. Dyn.*, *20*, 583–612, doi:10.1007/s00382-002-0296-y.

Lawrence, M. G., R. von Kuhlmann, M. Salzmann, and P. J. Rasch (2003), The balance of effects of deep convective mixing on tropospheric ozone, *Geophys. Res. Lett.*, *30*(18), 1940, doi:10.1029/2003GL017644.

Li, D., and K. P. Shine (1995), A 4-dimensional ozone climatology for UGAMP models, internal report, U.K. Univ. Global Atmos. Modell. Prog. Univ. of Reading, U. K.

Logan, J. A. (1999), An analysis of ozonesonde data for the troposphere: Recommendations for testing three-dimensional models and development of a gridded climatology for tropospheric ozone, *J. Geophys. Res.*, *104*, 16,115–16,149.

Meijer, E. W., P. F. J. van Velthoven, D. W. Brunner, H. Huntrieser, and H. M. Kelder (2001), Improvement and evaluation of the parametrisation of nitrogen oxide production by lightning, *Phys. Chem. Earth*, *26*(8), 577–583.

Murphy, D. M., and D. W. Fahey (1994), An estimate of the flux of stratospheric reactive nitrogen and ozone into the troposphere, *J. Geophys. Res.*, *99*, 5325–5332.

Olivier, J. G. J., et al. (1996), Description of EDGAR version 2.0, *rep. 771060 002*, RIVM, Bilthoven, Netherlands.

Pitari, G., E. Mancini, and A. Bregman (2002), Climate forcing of subsonic aviation: Indirect role of sulfate particles via heterogeneous chemistry, *Geophys. Res. Lett.*, *29*(22), 2057, doi:10.1029/2002GL015705.

Pope, V. D., M. L. Gallani, P. R. Rowntree, and R. A. Stratton (2000), The impact of new physical parameterizations in the Hadley Centre climate model: HadAM3, *Clim. Dyn.*, *16*, 123–146.

Prather, M. J. (1994), Lifetimes and eigenstates in atmospheric chemistry, *Geophys. Res. Lett.*, *21*, 801–804.

Prather, M. J. (2002), Lifetimes of atmospheric species: Integrating environmental impacts, *Geophys. Res. Lett.*, *29*(22), 2063, doi:10.1029/2002GL016299.

Prather, M., et al. (1999), Potential climate change from aviation, in *IPCC Special Report on Aviation and the Global Atmosphere*, edited by J. E. Penner et al., pp. 185–215, Cambridge Univ. Press, New York.

Prather, M., et al. (2001), Atmospheric chemistry and greenhouse gases, in *Climate Change 2001: The Scientific Basis*, edited by J. T. Houghton et al., pp. 239–287, Cambridge Univ. Press, New York.

Price, C., J. Penner, and M. Prather (1997), NO_x from lightning: 1. Global distribution based on lightning physics, *J. Geophys. Res.*, *102*, 5929–5941.

Reay, D. S., D. B. Nedwell, and N. McNamara (2001), Physical determinants of methane oxidation capacity in a temperate soil, in *Air-Surface Exchange of Gases and Particles*, edited by D. Fowler, C. E. R. Pitcairn, and J.-W. Erisman, pp. 401–414, Kluwer Acad., Norwell, Mass.

Sanderson, M. G. (1996), Biomass of termites and their emissions of methane and carbon dioxide: A global database, *Global Biogeochem. Cycles*, *10*, 543–557.

Sanderson, M. G., W. J. Collins, R. G. Derwent, and C. E. Johnson (2003a), Simulation of global hydrogen levels using a Lagrangian three-dimensional model, *J. Atmos. Chem.*, *46*, 15–28.

Sanderson, M. G., C. D. Jones, W. J. Collins, C. E. Johnson, and R. G. Derwent (2003b), Effect of climate change on isoprene emissions and surface ozone levels, *Geophys. Res. Lett.*, *30*(18), 1936, doi:10.1029/2003GL017642.

Schimel, D., et al. (1996), Radiative forcing of climate change, in *Climate Change 1995: The Science of Climate Change*, edited by J. T. Houghton et al., pp. 65–132, Cambridge Univ. Press, New York.

Smith, K. A., et al. (2000), Oxidation of atmospheric methane in northern European soils, comparison with other ecosystems, and uncertainties in the global terrestrial sink, *Global Change Biol.*, *6*, 791–803.

Stevenson, D. S., C. E. Johnson, W. J. Collins, and R. G. Derwent (1997), The impact of aircraft nitrogen oxide emissions on tropospheric ozone studied with a 3D Lagrangian model including fully diurnal chemistry, *Atmos. Environ.*, *31*, 1837–1850.

Stevenson, D. S., C. E. Johnson, W. J. Collins, R. G. Derwent, K. P. Shine, and J. M. Edwards (1998), Evolution of tropospheric ozone radiative forcing, *Geophys. Res. Lett.*, *25*, 3819–3822.

Stevenson, D. S., C. E. Johnson, E. J. Highwood, V. Gauci, W. J. Collins, and R. G. Derwent (2003), Atmospheric impact of the 1783–84 Laki eruption: part I, Chemistry modelling, *Atmos. Chem. Phys.*, *3*, 487–507.

Taylor, K. E., D. Williamson, and F. Zwiers (2000), The sea surface temperature and sea-ice concentration boundary conditions for AMIP II simulations, *Rep. 60*, 25 pp., Prog. for Clim. Model Diag. and Intercomparison Lawrence Livermore Natl. Lab., Livermore, Calif.

Thompson, A. M., et al. (2003a), Southern Hemisphere Additional Ozonesondes (SHADOZ) 1998–2000 tropical ozone climatology: 1. Comparison with Total Ozone Mapping Spectrometer (TOMS) and ground-based measurements, *J. Geophys. Res.*, *108*(D2), 8238, doi:10.1029/2001JD000967.

Thompson, A. M., et al. (2003b), Southern Hemisphere Additional Ozonesondes (SHADOZ) 1998–2000 tropical ozone climatology: 2. Tropospheric variability and the zonal wave-one, *J. Geophys. Res.*, *108*(D2), 8241, doi:10.1029/2002JD002241.

Wild, O., M. J. Prather, and H. Akimoto (2001), Indirect long-term global radiative cooling from NO_x emissions, *Geophys. Res. Lett.*, *28*, 1719–1722.

Yonemura, S., S. Kawashima, and H. Tsurata (2000), Carbon monoxide, hydrogen, and methane uptake by soils in a temperate arable field and a forest, *J. Geophys. Res.*, *105*, 14,347–14,362.

W. J. Collins, C. E. Johnson, and M. G. Sanderson, Hadley Centre for Climate Prediction and Research, Met Office, FitzRoy Road, Exeter, Devon EX1 3PB, UK. (bill.collins@metoffice.com; colin.johnson@metoffice.com; mgsanderson@metoffice.com)

R. G. Derwent, rdscientific, 18 Kingsland Grange, Newbury, RG14 6LH Berkshire, UK. (r.derwent@btopenworld.com)

R. M. Doherty and D. S. Stevenson, Institute of Atmospheric and Environmental Science, James Clerk Maxwell Building, King's Buildings, The University of Edinburgh, Edinburgh, Scotland EH9 3JZ, UK. (ruth@met.ed.ac.uk; dstevens@met.ed.ac.uk)

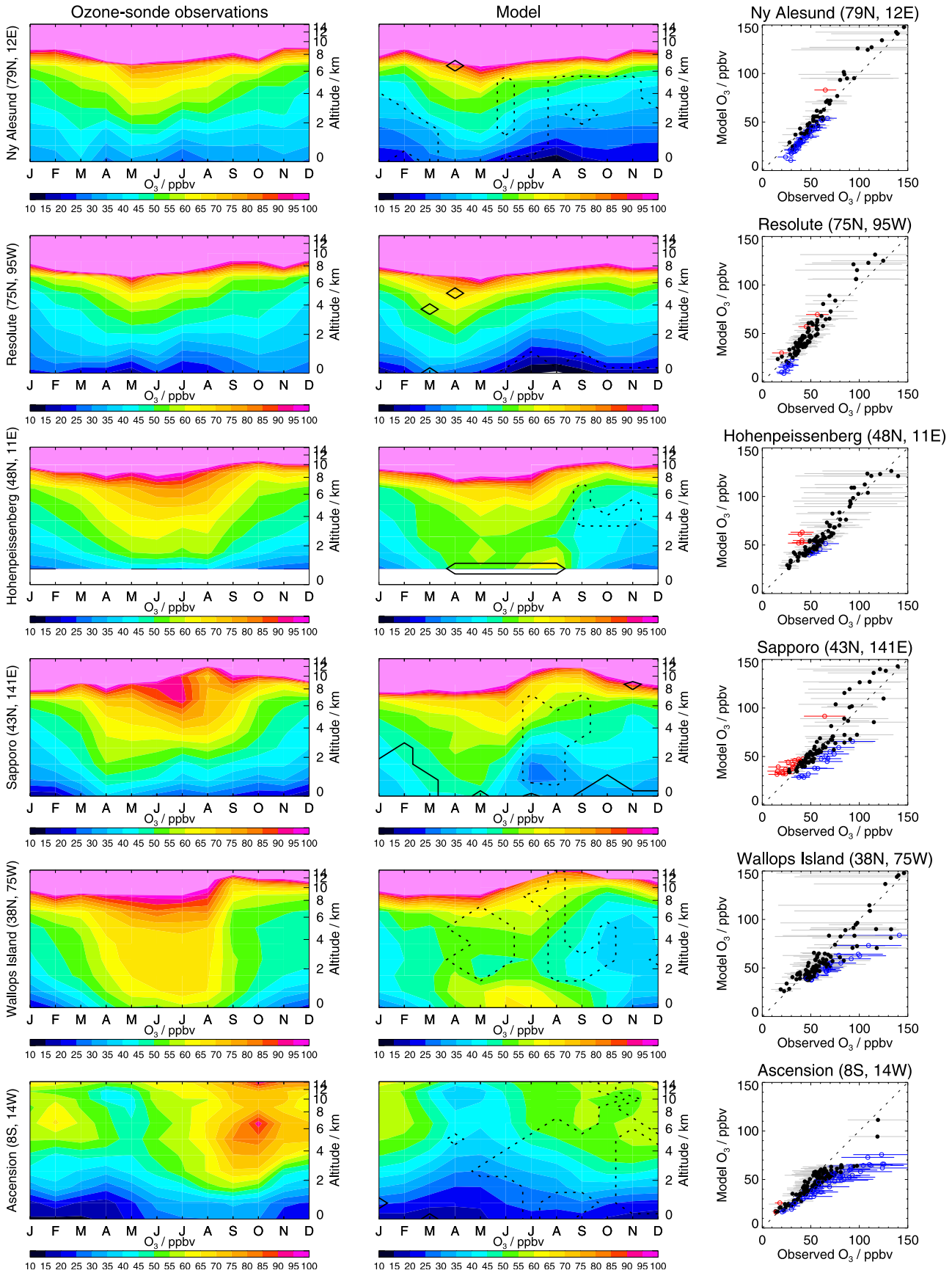
Ozone-sonde observations
Model
Ny Alesund (79N, 12E)
Resolute (75N, 95W)
Hohenpeissenberg (48N, 11E)
Sapporo (43N, 141E)
Wallops Island (38N, 75W)
Ascension (8S, 14W)
Altitude / km
J F M A M J J A S O N D
O3 / ppbv
10 15 20 25 30 35 40 45 50 55 60 65 70 75 80 85 90 95 100
Model O3 / ppbv
Observed O3 / ppbv
0 50 100 150

Figure 1

Figure 1. Comparison of O_3 from the control experiment with ozonesonde observations at six sites. The first column shows observations from *Logan* [1999] and *Thompson et al.* [2003a, 2003b]. The second column is the equivalent plot from the model, with a minor adjustment made to the vertical coordinate so that the height of the O_3 = 150 ppbv contour in the model is aligned with the same contour in the observations. This accounts for any mismatch between the modeled and observed tropopause height. The final column compares all points, with bars indicating the standard deviation in the observations. Where the model overpredicts (underpredicts) observations by more than one standard deviation, the point is plotted with an open symbol in red (blue); these points are shown in the second column by the solid (dashed) contours.

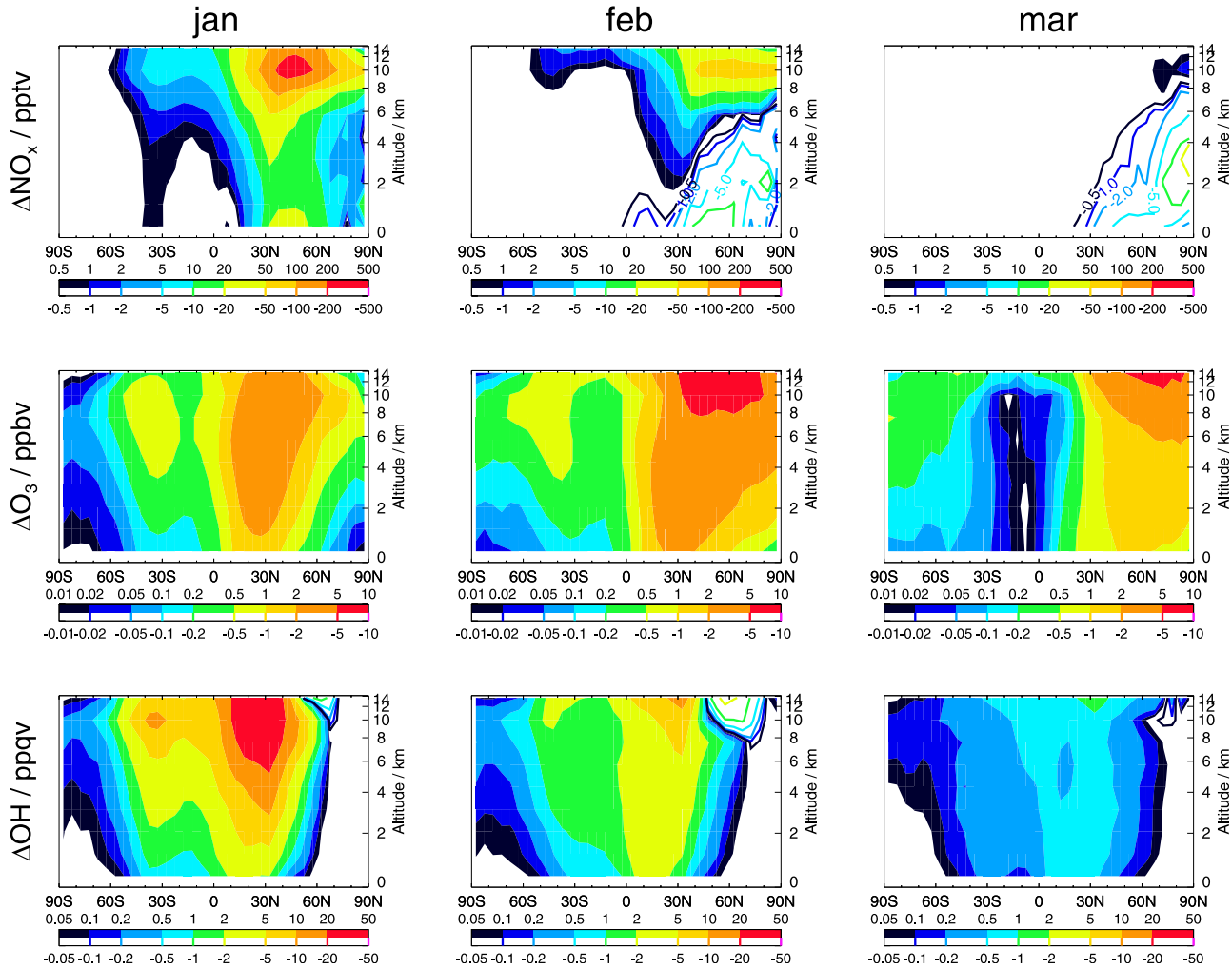

Figure 4. Monthly mean, zonal mean perturbations to (top) NO_x (pptv), (middle) O_3 (ppbv), and (bottom) OH (ppqv (parts per 10^{15} by volume)) in (left) January, (center) February, and (right) March for the January aircraft emissions pulse experiment. Filled contours show increases, and open contours show decreases. Emissions pulses in other months display similar responses.

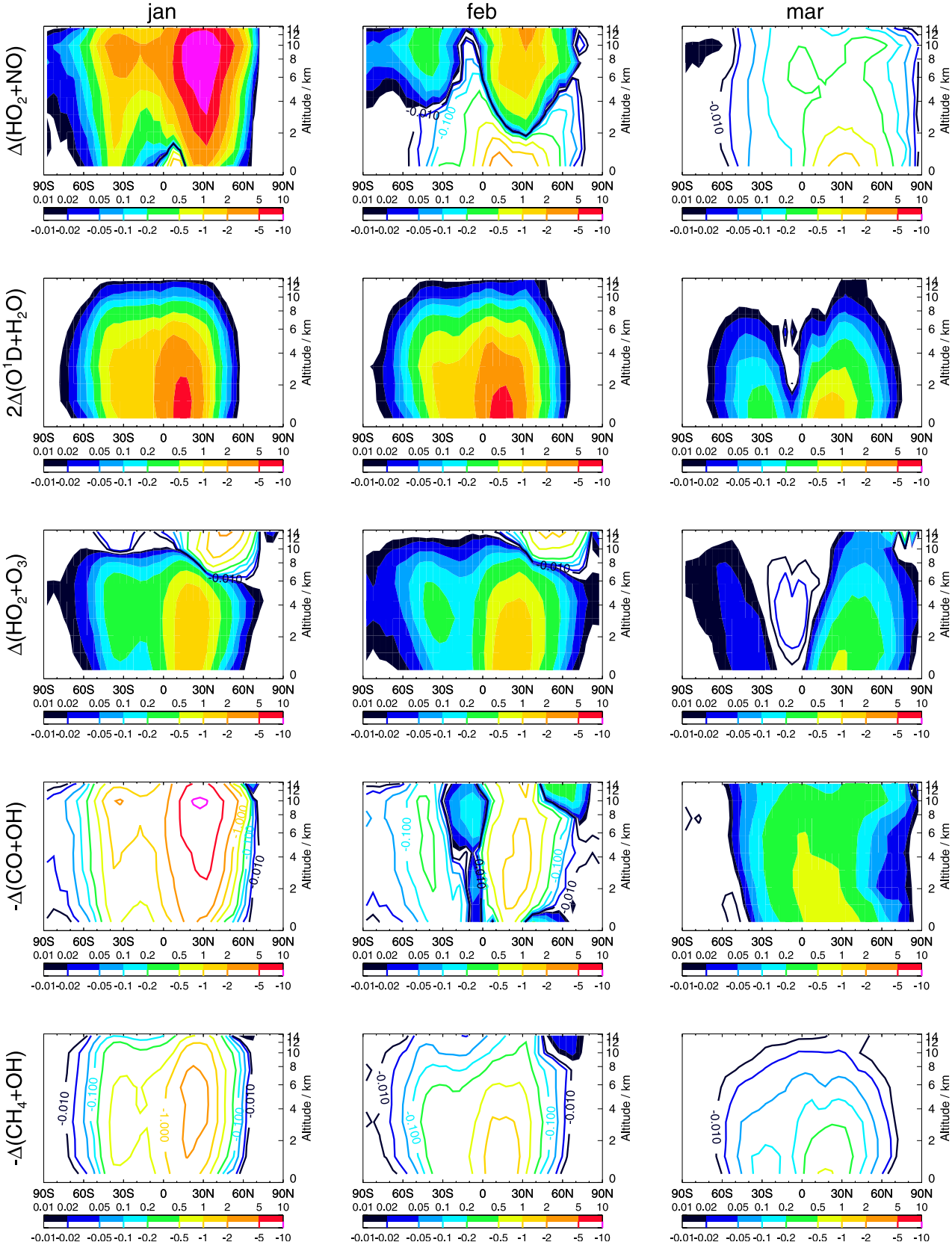

Figure 5. Monthly zonal mean perturbations to the major OH production and loss fluxes (ppbv/month) for the three months during/following the January emissions pulse. The two lowest rows show perturbations to OH loss reactions (4) and (5) and are multiplied by −1. Hence filled contours represent OH production, and open contours represent OH destruction. Emissions pulses in other months display similar responses.